

Analysis on the cation distribution of $Mg_xNi_{1-x}Fe2O4$ (x = 0, 0.25, 0.5, 0.75, 1) using Mössbauer spectroscopy and magnetic measurement

Shiyu Xu(徐诗语), Jiajun Mo(莫家俊), Lebin Liu(刘乐彬), and Min Liu(刘敏)
Citation: Chin. Phys. B, 2023, 32 (**12**): 127507. DOI: 10.1088/1674-1056/acca0c
Journal homepage: http://cpb.iphy.ac.cn; http://iopscience.iop.org/cpb

What follows is a list of articles you may be interested in

Magnetic properties and magnetocaloric effect of the Cr-based spinel sulfides $Co_{1-x}Cu_xCr_2S_4$

Xiao-Chao Zheng(郑小超), Xi-Yang Li(李西阳), Lun-Hua He(何伦华), Shao-Ying Zhang(张绍英), Ming-Hua Tang(唐明华), Fang-Wei Wang(王芳卫)
Chin. Phys. B, 2017, 26 (**3**): 037502. DOI: 10.1088/1674-1056/26/3/037502

First-principles investigation of electronic structure, effective carrier masses, and optical properties of ferromagnetic semiconductor $CdCr_2S_4$

Xu-Hui Zhu(朱旭辉), Xiang-Rong Chen(陈向荣), Bang-Gui Liu(刘邦贵)
Chin. Phys. B, 2016, 25 (**5**): 057501. DOI: 10.1088/1674-1056/25/5/057501

Effects of Mg substitution on the structural and magnetic properties of $Co_{0.5}Ni_{0.5-x}Mg_xFe_2O_4$ nanoparticle ferrites

R M Rosnan, Z Othaman, R Hussin, Ali A Ati, Alireza Samavati, Shadab Dabagh, Samad Zare
Chin. Phys. B, 2016, 25 (**4**): 047501. DOI: 10.1088/1674-1056/25/4/047501

Structure, morphology, and magnetic properties of high-performance NiCuZn ferrite

He Xue-Min (何学敏), Yan Shi-Ming (颜士明), Li Zhi-Wen (李志文), Zhang Xing (张星), Song Xue-Yin (宋雪银), Qiao Wen (乔文), Zhong Wei (钟伟), Du You-Wei (都有为)
Chin. Phys. B, 2015, 24 (**12**): 127502. DOI: 10.1088/1674-1056/24/12/127502

A new aluminum iron oxide Schottky photodiode designed via sol-gel coating method

A. Tataroğlu, A. A. Hendi, R. H. Alorainy, F. Yakuphanoğlu
Chin. Phys. B, 2014, 23 (**5**): 057504. DOI: 10.1088/1674-1056/23/5/057504

Analysis on the cation distribution of $Mg_xNi_{1-x}Fe_2O_4$ ($x = 0$, 0.25, 0.5, 0.75, 1) using Mössbauer spectroscopy and magnetic measurement

Shiyu Xu(徐诗语)[1,2], Jiajun Mo(莫家俊)[1], Lebin Liu(刘乐彬)[1], and Min Liu(刘敏)[1,3,†]

[1] *College of Nuclear Science and Technology, University of South China, Hengyang* 430074, *China*
[2] *School of Physics, Huazhong University of Science and Technology, Wuhan* 421001, *China*
[3] *Zhuhai Tsinghua University Research Institute Innovation Center, Zhuhai* 519000, *China*

(Received 26 February 2023; revised manuscript received 31 March 2023; accepted manuscript online 4 April 2023)

$Mg_xNi_{1-x}Fe_2O_4$ ($x = 0$, 0.25, 0.5, 0.75, 1) spinel ferrite material was analyzed to determine its magnetic properties and structure. X-ray diffraction (XRD), Mössbauer spectroscopy, and vibrating sample magnetometer (VSM) characterization were performed on the samples prepared using the sol–gel method. The results from XRD confirmed the existence of the single-phase cubic spinel structures $Fd\bar{3}m$, as well as the evolution of the crystalline size (D), the lattice parameter (a) and cell volume in compounds. The Mössbauer spectra showed the distribution of cations and changes in the magnetic properties of the sample. VSM measurement revealed that the samples were room-temperature ferromagnetic. Moreover, the saturation magnetization (M_s) of the samples changed with the Mg^{2+} ion content x, and a maximum occured at $x = 0.5$. Doping with Mg^{2+} ions increased the transfer of Ni^{2+} ions to tetrahedral sites, thus increasing the magnetic moment difference between tetrahedral (A) and octahedral (B) sites. Specifically, doping $NiFe_2O_4$ with Mg^{2+} ions can enhance its magnetic properties and enhance its saturation magnetization.

Keywords: spinel structure, magnetic properties, ferrite, Mössbauer spectra

PACS: 75.50.–y, 07.55.Jg **DOI:** 10.1088/1674-1056/acca0c

1. Introduction

Considerable attention has been given to spinel ferrite, the ferrite with the general formula MFe_2O_4 (M are divalent ions, such as Mn^{2+}, Ba^{2+}, Mg^{2+}, Co^{2+}, Cu^{2+}, Ni^{2+}, Zn^{2+}, Co^{2+}).[1] Historically, it has been used in many fields due to its high resistivity, chemical stability, mechanical hardness, and reasonable cost, including in information storage systems, magnetic cores, magnetic fluids, microwave absorbers, and many others.[2,3]

Spinels belong to the close packing with spatial symmetry group ($Fd\bar{3}m$), which is a relatively complex face-centered cubic (FCC) structure.[4] There are eight tetrahedral sites (A-sites) formed by four oxygen ions and 16 octahedral sites (B-sites) formed by six oxygen ions in each unit cell.[5] Within the spinel ferrite crystal structure, distinct cations exhibit distinct site selectivity (for example, Ni^{2+} ions tend to occupy octahedral sites, while Zn^{2+} ions tend to occupy tetrahedral sites). The ionic radius, the bonding type, and the preparation method determine the site preference.[6] Hence, the chemical formula structure of spinel ferrites is generally expressed as $(Fe^{3+}_{\delta}M^{2+}_{1-\delta})[M^{2+}_{\delta}Fe^{3+}_{2-\delta}]O_4$. where the round brackets ( ) mean tetrahedral site coordination and [ ] brackets mean octahedral site coordination.[7] The δ is a parameter that describes the inversion degree, which is the proportion of Fe^{3+} cations occupying tetrahedral sites in the spinel ferrite crystal structure.[8] The spinel crystal structure can be divided into three distinct structures based on the variation in the degree of inversion. The normal spinel structure, with $ZnFe_2O_4$ as a typical example, is characterized by the complete occupation of tetrahedral sites by Zn cations within the spinel crystal structure. Its chemical formula can be expressed as $(Zn^{2+})[Fe^{3+}_2]O_4$.[9] The mixed spinel structure, exemplified by $MgFe_2O_4$, is characterized by the partial occupation of both tetrahedral and octahedral sites by Mg cations within the spinel crystal structure. Its chemical formula is represented as $(Fe^{3+}_{\delta}Mg^{2+}_{1-\delta})[Mg^{2+}_{\delta}Fe^{3+}_{2-\delta}]O_4$.[10] In the inverse spinel ferrite structure, as seen in $NiFe_2O_4$, all Ni cations occupy octahedral sites within the spinel crystal structure, forming an $(Fe^{3+})[Ni^{2+}Fe^{3+}]O_4$ structure.[7] Ferrite's magnetic properties are determined by its cation distribution. Depending on the type and distribution of its cations, ferrite may be ferromagnetic, antiferromagnetic, or paramagnetic.[11]

$NiFe_2O_4$ is an inverse spinel ferrite that is also a known soft ferrite.[12] Due to its high-frequency permeability, high resistance, and low dielectric loss, it is widely used in high-frequency electronics.[3] The electromagnetic properties of Ni ferrite can be improved by ion doping, making it more practical.[13] The magnetic moments of Fe^{3+} ions and Ni^{2+} ions are 5 μ_B and 2 μ_B, respectively. Based on the A–B superexchange interaction, $NiFe_2O_4$ has a theoretical magnetic moment of 2 μ_B.[14,15]

Ni–Mg ferrite is a widely used type of soft magnetic ma-

†Corresponding author. E-mail: liuhart@126.com

© 2023 Chinese Physical Society and IOP Publishing Ltd

terial, but the structure and electromagnetic properties of Mg ferrite are different from those of Ni ferrite. This is because Mg^{2+} cations have a certain preference for octahedral sites, but this preference is weaker than that of Ni cations.[16] Also, Mg^{2+} ions have a diamagnetic moment (0 μ_B); therefore, the superexchange interaction with iron ions is different from that with Ni^{2+} ions.[15] It is also important to note that the position preferences and ionic radii of Ni^{2+} ions and Mg^{2+} ions are also different, which affect the magnetic properties of Mg–Ni ferrite. In this way, Ni–Mg ferrite can be optimized for outstanding properties by changing the proportion of Ni^{2+} ions and Mg^{2+} ions.

We prepared Mg–Ni spinel ferrite materials, $Mg_xNi_{1-x}Fe_2O_4$ ($x = 0$, 0.25, 0.5, 0.75, 1), using the sol–gel method in this study. Tests were performed on samples using x-ray diffractometers, Mössbauer spectrometers, and vibrating sample magnetometers. Different properties were fitted and analyzed based on x-ray diffraction (XRD), Mössbauer spectra, and vibrating sample magnetometer (VSM) data, and the cation distribution and magnetic changes were determined.

2. Experimental techniques

2.1. Sample preparation

In this work, Mg–Ni spinel ferrites, $Mg_xNi_{1-x}Fe_2O_4$ ($x = 0$, 0.25, 0.5, 0.75, 1), were prepared using the sol–gel method. The raw materials iron(III) nitrate nonahydrate $Fe(NO_3)_3{\cdot}9H_2O$, nickel(II) nitrate hexahydrate $Ni(NO_3)_2{\cdot}6H_2O$, magnesium(II) nitrate hexahydrate $Mg(NO_3)_2{\cdot}6H_2O$ and citric acid $C_6H_8O_7$ were purchased from Macklin. A calculation was made to determine the amount of raw materials required for the experiment. One mole of spinel ferrite requires three moles of nitrate and three moles of citric acid. The desired quantities of reagents were dissolved in 150 ml of deionized water and heated at 80 °C. Ammonia was gradually added to the compound solution while stirring to maintain a pH of 7–9. The solution was stirred for 5 h until it evaporated to produce a highly viscous gel. This gel was then baked at 225 °C for 4 h, resulting in foamy ferrite powder. A dense ceramic metal oxide is formed by grinding the oxide into a fine powder, then calcining it at 1000 °C for 9 h in a muffle furnace. Finally, the calcined metal oxide is ground in a mortar to obtain the finished product.[12]

2.2. Characterization of the samples

The XRD patterns of samples were recorded using a Siemens D500 diffractometer with Cu α ($\lambda = 1.5418$ Å) radiation, which is in a Bragg angle range ($10° \leq \theta \leq 80°$). The patterns were analyzed using MDI-JADE software. The Mössbauer spectra were obtained at room temperature by a Seeco W304 Mössbauer spectrometer with a ^{57}Co/Rh source. Spectra were fitted using Mosswinn 4.0 software, and the most appropriate parameters were estimated. A magnetization curve (M–H) for the compounds was determined from VSM measurements at temperatures of 300 K and 5 K, respectively, and from −7 T to 7 T external magnetic field.

3. Results and discussion

3.1. X-ray diffraction analysis

The XRD data of Mg–Ni spinel ferrite $Mg_xNi_{1-x}Fe_2O_4$ ($x = 0$, 0.25, 0.5, 0.75, 1) with different Mg^{2+} ion contents are shown in Fig. 1. The XRD patterns of the synthesized materials are shown in Figs. 1(a)–1(e), respectively, and those of $NiFe_2O_4$ (PDF: # 97-005-2387) and $MgFe_2O_4$ (PDF:# 97-004-0679) in the PDF file are shown in Figs. 1(f) and 1(g). The patterns of the materials prepared in the experiment are generally consistent with those of the standard JCPDS cards. Each sample showed identical peaks of planes (220), (331), (400), (422), (511) and (440). Therefore, the single-phase cubic spinel structure $Fd\bar{3}m$ is formed, and all the compounds are spinel ferrites with a face-centered cubic structure.[1]

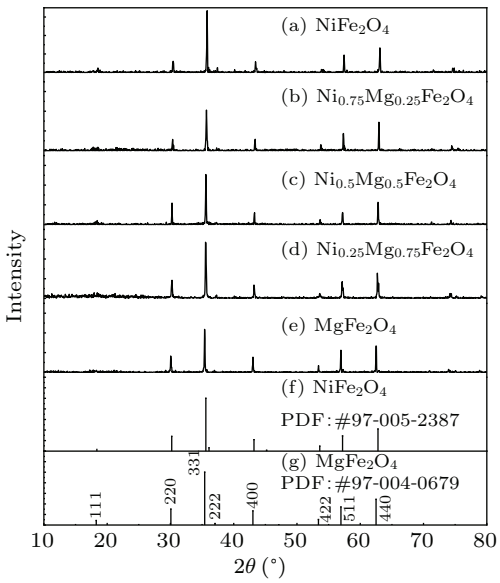


Fig. 1. Powder XRD patterns of spinel $Mg_xNi_{1-x}Fe_2O_4$ ($x = 0$, 0.25, 0.5, 0.75, 1) powers.

Using the type of diffraction peak and intensity of the diffraction ray, it is possible to calculate the crystallite size (D), the lattice parameter (a), and cell volume of the samples. Based on the Scherrer equation, the crystallite size (D) of the samples was estimated by[17]

$$D = k\lambda/(\beta\cos\theta), \tag{1}$$

where k is a constant (the value is usually 0.9), β is the half intensity width of the different peaks, λ is the x-ray wavelength, and θ is the angle of diffraction.

The lattice constant a (Å) is calculated from the Nelson–Riley correction and Bragg equation[18]

$$a = \lambda\sqrt{h^2+k^2+l^2}/(2\sin\theta), \tag{2}$$

where λ is the x-ray wavelength, h, k, and l are the Miller indices, and θ is the angle of diffraction.

Based on the calculated microcrystalline size (D), lattice parameter (a) and cell volume of the samples. The lattice constant increases from 8.3 Å to 8.4 Å, within the range of spinel ferrite lattice constants. Grain sizes range from 10 nm to 100 nm, which are larger nanoparticles. The cell volume ranges from 580 Å^3 to 600 Å^3, which is within the normal range of Ni–Mg spinel ferrites. The preparation of Ni–Mg spinel ferrite appears to be successful.

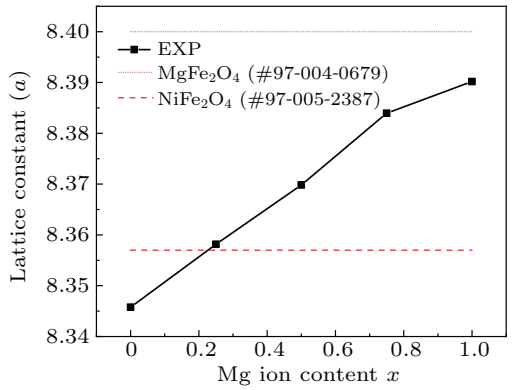


Fig. 2. The evolution of the lattice constant of the samples and standard lattice constants of $NiFe_2O_4$ and $MgFe_2O_4$.

As it appears on the standard JCPDS cards ($NiFe_2O_4$: #97-005-2387; $MgFe_2O_4$: #97-004-0679), $NiFe_2O_4$ has a lattice constant of $a = b = c = 8.34577$ Å, and $MgFe_2O_4$ has a lattice constant of $a = b = c = 8.3998$ Å. Standard cards are compared with the calculated results of the experimental data for lattice constants. The lattice constants of the samples and the standard $NiFe_2O_4$ and $MgFe_2O_4$ are shown in Fig. 2. It can be seen that the samples' lattice constants increase as the amount of Mg^{2+} increases. The lattice constant of the samples increases with increasing Mg^{2+} ion content since the radii of Ni^{2+} ions and Mg^{2+} ions at octahedral positions are 0.069 nm and 0.072 nm, respectively.[19] The lattice constants of synthesized $NiFe_2O_4$ and $MgFe_2O_4$ differ slightly from those of the standard JCPDS card. According to Msomi *et al.*'s [20] study on Co–Ni spinel ferrite, lattice constants have a relationship with annealing temperatures. The lattice constant first increases (200–700 °C) and then decreases (700–1100 °C) as the annealing temperature increases (200–1100 °C). Thus, it is speculated that the higher annealing temperature may have caused the difference in lattice constants between the sample and the standard JCPDS cards. An increase in lattice constant is observed with changes in Mg ion content, which is consistent with the results reported by Rosnan *et al.* This implies successful Mg^{2+} ion doping.[21]

3.2. Mössbauer spectroscopy analysis

Due to the strong preference of Ni^{2+} ions for octahedral sites, two sextets were used to fit the Mössbauer spectrum data of the $NiFe_2O_4$ sample. The results of the fitting and the associated parameters are shown in Table 1 and Fig. 3(a). The obtained results indicate that the peak area of iron ions in the tetrahedral sites (I_A) is 47.5%, while that in the octahedral sites (I_B) is 52.5%. The positions of cations can be calculated by I_A and I_B using the following formula:[22]

$$\frac{I_B}{I_A} = \frac{2-\delta}{\delta} \times \frac{f_{FeB}}{f_{FeA}}, \tag{3}$$

where δ is the inversion degree in $(Fe^{3+}_{\delta}Mg^{2+}_{1-\delta})[Mg^{2+}_{\delta+x-1}Ni_{1-x}Fe^{3+}_{2-\delta}]O_4$, and f_{FeB} and f_{FeA} are the recoilless f-factors for the tetrahedral (A) and the octahedral (B) sites. The value of f_{FeB}/f_{FeA} in Ni ferrite is 1.09. The calculation results suggest that 99.3% of Ni ions occupy octahedral sites, indicating the nearly perfect inverse spinel structure of the sample, which is consistent with the results reported in other studies.[23]

$Mg_xNi_{1-x}Fe_2O_4$ ($x = 0.25, 0.5, 0.75, 1$) has a more complicated cation distribution due to the addition of Mg^{2+} ions. Some approximations are introduced to simplify the calculation. For the octahedral sites of Fe^{3+} ions, a sextet (labeled as sextet A) was used for fitting. For the tetrahedral sites of Fe^{3+} ions, a study found that the dominant superexchange interaction for Fe^{3+} ions at octahedral sites is the interaction between A-sites and B-sites: (A)–O–[B]. Because it is 15–20 times stronger than the interaction between B-sites and B-sites, only the superexchange between B-sites and A-sites is considered.[23] Tetrahedral sites are considered to contain no nickel ions, since Ni^{2+} ions prefer octahedral sites. Due to the trivalent Fe ions in the sample, the structure has extremely high symmetry, quadruple splitting (QS) = 0 mm/s and isomer shift (IS) = 0–0.5 mm/s. Many studies[24,25] have reported that the Mössbauer spectroscopic parameters of Fe ions at the B site are influenced by the six nearest tetrahedral sites of cations. Depending on the fraction of Mg^{2+} ions at these tetrahedral sites surrounding the Fe ions, different sextets can be observed, denoted as B, B_1, ..., B_n, where n is the number of Mg^{2+} ions among the six nearest tetrahedral sites. The probability of observing a certain sextet at the octahedral site $P(n,a)$ can be expressed as a function of the number of Mg^{2+} ions among the six nearest tetrahedral sites (n) using the following equation:

$$p(n,a) = C_6^n \times a^n \times (1-a)^{6-n}, \tag{4}$$

where a is the Mg^{2+} ion content of the A-site. $P(n,a)$ values lower than 5% contribute very little to Mössbauer spectra and can be omitted.[9] Some papers[16] define a as the total amount of Mg ions x, but many studies have shown that $MgFe_2O_4$ is

a disordered spinel ferrite and the value of a does not equal x.[19,26] Therefore, in this study, the fitting of the Mössbauer spectra for B-sites is not solely based on Eq. (4). Mössbauer spectrum data of $Mg_xNi_{1-x}Fe_2O_4$ with $x = 0.25$, 0.5, 0.75, and 1 were fitted starting from two sextets. The value of $(1 - I_A)$ from the fitting was used as the actual Mg^{2+} ion content a for the A-sites, which was then substituted into Eq. (4). The probability given by Eq. (4) was compared with the fitted peak areas (I_{rel}), and a set of better fitting results was chosen as the final results. This results in four, five, five, and six sextets in the samples with $x = 0.25$, 0.5, 0.75, and 1, as shown in Fig. 3 and Table 1.

There was substantial agreement between the fitted curve and the experimental data. The crystal blocking temperature is a size-dependent parameter.[27] When the blocking temperature of the crystal falls below test temperature, the thermal energy exceeds the anisotropic energy, and the samples display superparamagnetic behavior. It appears that the Mössbauer spectrum is a doublet or a collapse of the Mössbauer spectroscopy. The absence of these appearances suggests the synthesized sample has a large grain size, which is consistent with the XRD data. The values of the isomer shift are between 0.1 mm/s and 0.5 mm/s, with the B-site generally higher than the A-site, consistent with other studies.[26]

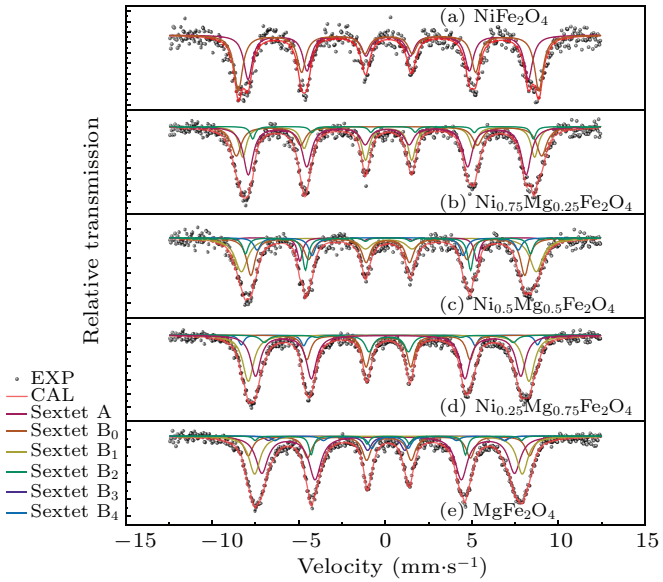


Fig. 3. Room-temperature ^{57}Fe Mössbauer spectra of spinel $Mg_xNi_{1-x}Fe_2O_4$ ($x = 0$, 0.25, 0.5, 0.75, 1) powers. Here, EXP and CAL are experimental and computational Mössbauer data, respectively.

Table 1. Mössbauer parameters of spinel $Mg_xNi_{1-x}Fe_2O_4$ ($x = 0$, 0.25, 0.5, 0.75, 1) powers. Here, IS is isomer shift, Γ is the Lorentzian linewidth, H_{eff} is the hyperfine magnetic field, I_{rel} is relative areas and cations at A and B sites.

x	Site	Γ (mm/s)	IS (mm/s)	H_{eff} (T)	I_{rel}	Cations at A site	Cations at B site
0	A	0.62	0.17	50.32	47.50%	$Fe_{0.993}Ni_{0.007}$	$Fe_{1.007}Ni_{0.993}$
	B	0.62	0.20	53.96	52.50%		
0.25	A	0.66	0.11	49.85	43.00%	$Fe_{0.903}Mg_{0.097}$	$Fe_{1.097}Ni_{0.75}Mg_{0.153}$
	B	0.70	0.21	54.80	22.00%		
	B_1	0.52	0.20	52.41	29.50%		
	B_2	0.34	0.45	50.39	5.50%		
0.5	A	0.59	0.15	49.17	36.90%	$Fe_{0.779}Mg_{0.221}$	$Fe_{1.221}Ni_{0.5}Mg_{0.279}$
	B	0.37	0.18	54.89	7.80%		
	B_1	0.89	0.20	52.93	29.70%		
	B_2	0.38	0.16	51.20	14.90%		
	B_3	0.48	0.14	46.89	10.70%		
0.75	A	0.69	0.17	47.62	40.00%	$Fe_{0.842}Mg_{0.158}$	$Fe_{1.158}Ni_{0.25}Mg_{0.592}$
	B	0.76	0.20	50.40	24.00%		
	B_1	0.53	0.18	50.62	20.50%		
	B_2	0.57	0.20	44.67	10.20%		
	B_3	0.37	0.24	53.17	5.30%		
1	A	0.83	0.17	45.36	40.40%	$Fe_{0.850}Mg_{0.150}$	$Fe_{1.150}Mg_{0.850}$
	B	0.58	0.21	50.51	23.20%		
	B_1	0.78	0.19	48.05	18.10%		
	B_2	0.32	0.18	47.85	6.10%		
	B_3	0.54	0.06	42.25	6.10%		
	B_4	0.48	0.27	41.29	6.20%		

Based on the relative areas of the tetrahedral site I_A and octahedral site I_B, we can calculate the distribution of Fe^{3+} ions. As a result, it gives the cations at A and B sites of $Mg_xNi_{1-x}Fe_2O_4$ ($x = 0$, 0.25, 0.5, 0.75, 1), as shown in Table 1. As is evident, Ni^{2+} ion content influences Mg^{2+} ion proportions in tetrahedral sites. When Ni^{2+} ions are abundant, Mg^{2+} ions tend to occupy tetrahedral sites. Furthermore, the distribution of different cations causes different magnetic properties; therefore, it is possible to calculate the saturation magnetic moments of a whole series of samples.[28] The relationship between the saturation magnetic moment and the cation distribution can be calculated using the following for-

mula for each chemical formula of the sample:[29]

$$\mu_x^{\mathrm{CAL}} = \{(1-x)\times\mu_{\mathrm{Ni}} + (2-\delta)\times\mu_{\mathrm{Fe}}\} - [\delta\times\mu_{\mathrm{Fe}}], \quad (5)$$

where the notation { } represents the magnetic moment at the B site, and [ ] represents the magnetic moment at the A site. Here, μ_{Ni} and μ_{Fe} are 2 μ_{B} and 5 μ_{B}, respectively, and δ is the inversion degree in $(Fe_{\delta}^{3+}Mg_{1-\delta}^{2+})[Mg_{\delta+x-1}^{2+}Ni_{1-x}Fe_{2-\delta}^{3+}]O_4$. The calculation results are presented in Table 2 and Fig. 4. CAL. With increasing x, the sample's saturation magnetization first increases and then decreases. The trend of the variation of the saturation magnetization is similar to the trend of the doping non-magnetic ion Zn in $CoFe_2O_4$.[30] When the value of x is between 0.25 and 0.5, the results of the Mössbauer spectroscopy show a significant number of Mg ions located in the tetrahedral position, which is consistent with previous studies:[19] Ni^{2+} ions prefer octahedral positions more than Mg^{2+} ions, resulting in more non-magnetic Mg^{2+} ions occupying tetrahedral positions. Consequently, the total magnetic moment of tetrahedral sites decreases, and the saturation magnetic moment difference between tetrahedral and octahedral sites becomes greater. As x reaches 0.5, the saturated magnetic moment reaches its maximum value. Afterwards, with the continued increase in Mg^{2+} ions, the non-magnetic Mg^{2+} ions occupying octahedral sites increase and the Ni^{2+} ions decrease, leading to a rapid decrease in the total saturated magnetic moment within octahedral sites. The difference in the saturation magnetic moment between A and B sites decreases, which makes the saturation magnetic moment of the samples drop continuously. A sample's saturation magnetic moment ceaselessly decreases before its Ni^{2+} ion content reaches zero. The evolution of the saturated magnetic moment and Mg^{2+} ion content x clearly demonstrates the correlation between structure and magnetic properties.

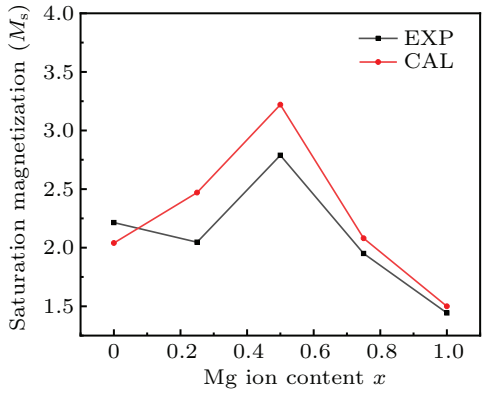


Fig. 4. The experimental (EXP) and computational (CAL) saturation magnetic moment of spinel $Mg_xNi_{1-x}Fe_2O_4$ ($x = 0$, 0.25, 0.5, 0.75, 1) powers.

Table 2. The experimental and computational saturation magnetic moment of spinel $Mg_xNi_{1-x}Fe_2O_4$ ($x = 0$, 0.25, 0.5, 0.75, 1) powers.

x	0	0.25	0.5	0.75	1
CAL (μ_{B})	2.04	2.47	3.22	2.08	1.5
EXP (μ_{B})	2.21	2.05	2.79	1.95	1.44

3.3. Vibrating sample magnetometer analysis

Data on the magnetization of the compounds were collected using VSM and are plotted in Figs. 5 and 6. The data show typical ferromagnetic behavior at 5 K and 300 K, suggesting that the Curie temperature of the sample is higher than 300 K. The maximum saturation magnetization (M_{s}) was calculated using the following equation by using the hysteresis loop:[31]

$$\mu_x^{\mathrm{EXP}} = \sigma_{\mathrm{s}} \times \frac{M_x}{5585}\mu_{\mathrm{B}}, \quad (6)$$

where σ_{s} is the saturation magnetization intensity in the hysteresis loop at 5 K, and M_x is the relative molecular weight of the material. The calculated results are shown in Table 2 and Fig. 4. EXP. As the Mg ion content increases, the saturation magnetization decreases from 2.21 μ_{B} to 2.04 μ_{B}, then increases to 2.79 μ_{B}, and finally decreases to 1.44 μ_{B}. The experimental and computational saturation magnetic moments of the compounds are compared in Fig. 4. It is evident that both sets of data show a similar change trend, even though the theoretical data is higher than the experimental data when Mg and Ni ions coexist. The discrepancy between the experimental and theoretical data at $x = 0$, 0.25, 0.5, and 0.75 may arise from

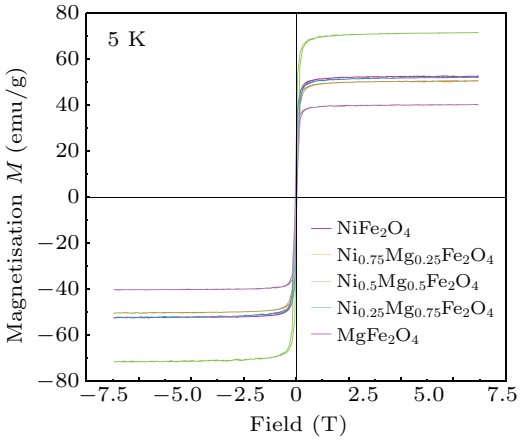


Fig. 5. Magnetic hysteresis (M–H) loops of spinel $Mg_xNi_{1-x}Fe_2O_4$ ($x = 0$, 0.25, 0.5, 0.75, 1) powers at 5 K.

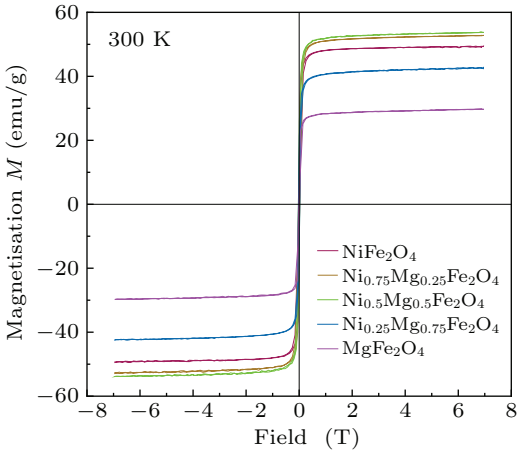


Fig. 6. Magnetic hysteresis (M–H) loops of spinel $Mg_xNi_{1-x}Fe_2O_4$ ($x = 0$, 0.25, 0.5, 0.75, 1) powers at 300 K.

the incomplete consideration of the distribution of Ni ions. Some Ni^{2+} ions may occupy tetrahedral sites, especially when the concentration of Ni^{2+} ions decreases. Some Ni^{2+} ions in octahedral sites may potentially exchange with Mg^{2+} ions in tetrahedral sites. As a result, the magnetic moment at tetrahedral sites increases, while the magnetic moment at octahedral sites decreases, leading to a smaller total magnetic moment.

4. Conclusions

In this work, $Mg_xNi_{1-x}Fe_2O_4$ ($x = 0$, 0.25, 0.5, 0.75, 1) spinel ferrite materials were successfully prepared using the sol-gel method, and their structure and magnetic properties were analyzed. Based on the results, it can be concluded that the structure and magnetism of the samples are affected by the Mg^{2+} ion content x. Extensive XRD analysis showed that the sample remained a cubic spinel structure $Fd\bar{3}m$ with an increase in Mg^{2+} ion content x. Because the Mg ion radius of octahedral sites is larger than the Ni ion radius, the crystallite size (D), lattice parameter (a), and cell volume gradually increase. According to the Mössbauer spectrum analysis, the distribution ratio of Fe^{3+} ions between octahedral sites and tetrahedral sites changes with a change in Mg^{2+} ion content x. Cations are distributed differently in different materials, resulting in different magnetic properties. Mössbauer spectral analysis data are used to calculate the saturation magnetization of the sample. The results indicate that with the change in Mg^{2+} ion content x, the saturation magnetization of the sample first increases from 2.04 μ_B to 3.22 μ_B, and then decreases to 1.5 μ_B. Based on the M–H curve at 5 K and 300 K, it is demonstrated that the sample is a ferromagnetic at room temperature. With an increase in Mg^{2+} ion content, the saturation magnetization decreases from 2.21 μ_B to 2.04 μ_B, then increases to 2.79 μ_B, and finally decreases to 1.44 μ_B. Experimental data and data calculated by structure show the same evolution trend, and the error may be caused by an incomplete consideration of Ni ion distribution.

Acknowledgements

Project supported by the National Natural Science Foundation of China (Grant No. 11447231), the National Undergraduate Innovation and Entrepreneurship Training Program Support Projects of China, the Natural Science Foundation of Hunan Province, China (Grant No. 2020JJ4517), the Research Foundation of the Education Bureau of Hunan Province, China (Grant Nos. 19A434, 19A433, and 19C1621), and the Opening Project of the Cooperative Innovation Center for Nuclear Fuel Cycle Technology and Equipment, University of South China (Grant Nos. 2019KFY10 and 2019KFY09).

References

[1] Dhaou M H, Hcini S, Mallah A, Bouazizi M L and Jemni A 2017 *Appl. Phys. A* **123** 1
[2] Gul I H, Ahmed W and Maqsood A 2008 *J. Magn. Magn. Mater.* **320** 270
[3] Mathew D S and Juang R S 2007 *Chem. Eng. J.* **129** 51
[4] Mocanu Z V, Airimioaei M, Ciomaga C E, Curecheriu L, Tudorache F, Tascu S, Iordan A R, Palamaru N M and Mitoseriu L 2014 *J. Mater. Sci.* **49** 3276
[5] Zhang Z J, Wang Z L, Chakoumakos B C and Yin J S 1998 *J. Am. Chem. Soc.* **120** 8380
[6] Phong P T, Nam P H, Phuc N X, Huy B T, Lu L T, Manh D H and Lee I J 2019 *Metall. Mater. Trans. A* **50** 1571
[7] Shang Z F, Qi W H, Ji D H, Xu J, Tang G D, Zhang X Y, *et al.* 2014 *Chin. Phys. B* **23** 107503
[8] Maazouzi A E, Masrour R, Jabar A and Hamedoun M 2019 *Chin. Phys. B* **28** 057504
[9] Sorescu M, Diamandescu L, Peelamedu R, Roy R and Yadoji P 2004 *J. Magn. Magn. Marer.* **279** 195
[10] Araújo J C R, Araujo-Barbosa S, Souza A L R, Iglesias C A M, Xavier J, Souza P B, *et al.* 2021 *J. Phys. Chem. Solids* **154** 110051
[11] Gherca D, Pui A, Cornei N, Cojocariu A, Nica V and Caltun O 2012 *J. Magn. Magn. Mater.* **324** 3906
[12] John Berchmans L, Kalai Selvan R, Selva Kumar P N and Augustin C O 2004 *J. Magn. Magn. Mater.* **279** 103
[13] Anantharamaiah P N, Rao B P, Shashanka H M, Chelvane J A, Khopkar V and Sahoo B 2021 *Phys. Chem. Chem. Phys.* **23** 1694
[14] Lüders U, Bibes M, Bobo J F, Cantoni M, Bertacco R and Fontcuberta J 2005 *Phys. Rev. B* **71** 134419
[15] Amer M A, Meaz T M, Attalah S S and Ghoneim A I 2014 *J. Magn. Magn. Mater.* **363** 60
[16] Mittal V K, Chandramohan P, Bera S, Srinivasan M P, Velmurugan S and Narasimhan S V 2006 *Solid State Commun.* **137** 6
[17] Hassan A, Azhar Khan M, Shahid M, Asghar M, Shakir I, Naseem S, *et al.* 2015 *J. Magn. Magn. Mater.* **393** 56
[18] Low Z H, Ismail I, Shafie M S E, Ibrahim I R, Ertuğrul M, Azis R S, *et al.* 2019 *Results Phys.* **15** 102683
[19] Airimioaei M, Palamaru M N, Iordan A R, Berthet P, Decorse C, Curecheriu L and Mitoseriu L 2014 *J. Am. Ceram Soc.* **97** 519
[20] Msomi J Z, Ndlovu B, Moyo T and Osman N S E 2016 *J. Alloys Compd.* **683** 149
[21] Rosnan R M, Othaman Z, Hussin R, Ati A A, Samavati A, Dabagh S and Zare S 2016 *Chin. Phys. B* **25** 047501
[22] Vitor P A M, Venturini J, da Cunha J B M and Bergmann C P 2021 *J. Alloys Compd.* **851** 156799
[23] Velinov N, Manova E, Tsoncheva T, Estournès C, Paneva D, Tenchev K, *et al.* 2012 *Solid State Sci.* **14** 1092
[24] Ferreira T A S, Waerenborgh J C, Mendonça M H R M, Nunes M R and Costa F M 2003 *Solid State Sci.* **5** 383
[25] G'omez C A P, Meneses C A B and Jaén J A 2020 *J. Magn. Magn. Mater.* **505** 166710
[26] Nakagomi F, da Silva S W, Garg V K, Oliveira A C, Morais P C and Franco A 2009 *J. Solid State Chem.* **182** 2423
[27] Sarkar K, Mondal R, Dey S and Kumar S 2020 *Physica B* **583** 412015
[28] Pradeep A and Chandrasekaran G 2006 *Mater. Lett.* **60** 371
[29] Lakhani V K, Trivedi U N, Vasoya N H, Raval P Y and Modi K B 2019 *Physica B* **570** 291
[30] Li W and Fa-Shen L 2008 *Chin. Phys. B* **17** 1858
[31] Adhlakha N and Yadav K L 2012 *Smart. Mater. Struct.* **21** 115021